Volume 10
Number 17
7 September 2020
Pages 5691–6077

Catalysis Science & Technology

rsc.li/catalysis

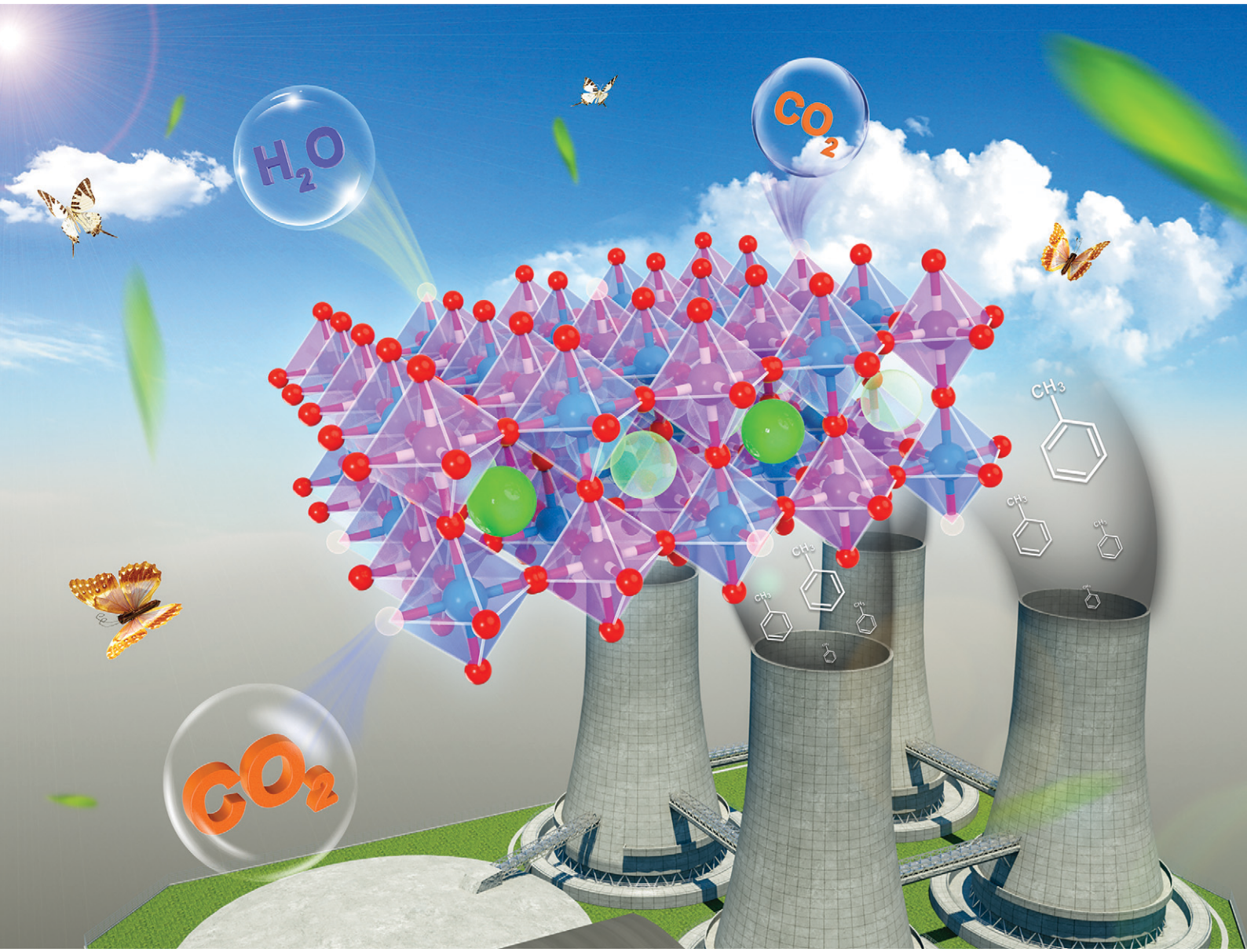

ISSN 2044-4761

ROYAL SOCIETY OF CHEMISTRY

PAPER

Xiaoliang Liang, Peng Liu *et al.*
Facile surface improvement of $LaCoO_3$ perovskite with high activity and water resistance towards toluene oxidation: Ca substitution and citric acid etching

Catalysis Science & Technology

ROYAL SOCIETY OF CHEMISTRY

PAPER

View Article Online
View Journal | View Issue

Cite this: *Catal. Sci. Technol.*, 2020, 10, 5829

Facile surface improvement of $LaCoO_3$ perovskite with high activity and water resistance towards toluene oxidation: Ca substitution and citric acid etching†

Hanlin Chen,[afg] Gaoling Wei,[bc] Xiaoliang Liang, *[afg] Peng Liu,*[d] Yunfei Xi [e] and Jianxi Zhu [afg]

Thermal catalytic oxidation is regarded as an effective technique to eliminate volatile organic compounds (VOCs), whereby perovskite-type oxides have been reported as low-cost and highly efficient transition metal catalysts. In this study, we employ two facile modification methods, *i.e.*, Ca substitution and citric acid etching, to further improve the catalytic activity of $LaCoO_3$ perovskite for toluene oxidation. The Ca-substituted $LaCoO_3$ ($La_{0.9}Ca_{0.1}CoO_3$) and citric acid-etched $LaCoO_3$ ($LaCoO_3$–CA) show T_{90} values at 220 and 215 °C, respectively, which are substantially lower than that of pristine $LaCoO_3$ (305 °C). When $LaCoO_3$ is modified by both Ca substitution and citric acid etching, *i.e.*, $La_{0.9}Ca_{0.1}CoO_3$–CA, the T_{90} further decreases to 202 °C, even lower than that of the commercial catalyst 0.5 wt% Pt/Al_2O_3 (208 °C). In terms of specific reaction rate at 200 °C, the activity of the above catalysts is also enhanced as follows: $LaCoO_3$ (0.14 μmol s^{-1} m^{-2}) < $La_{0.9}Ca_{0.1}CoO_3$ (0.31 μmol s^{-1} m^{-2}) < $LaCoO_3$–CA (0.47 μmol s^{-1} m^{-2}) < $La_{0.9}Ca_{0.1}CoO_3$–CA (0.63 μmol s^{-1} m^{-2}). The effects of Ca substitution and citric acid etching are discussed in light of the crystal structure, morphology, and lattice defects. On the one hand, Ca substitution and citric acid etching increase the specific surface area and pore volume, which facilitate the contact between toluene and active sites. On the other hand, these methods produce more oxygen vacancies, enhance the reducibility, and facilitate the adsorption of oxygen. The above merits result in the increase in the specific reaction rate. The modified catalysts show a better water resistance than pristine $LaCoO_3$. As verified in the H_2O-TPD characterization, this phenomenon is ascribed to the generation of surface hydroxyl groups, which are beneficial for toluene oxidation at high humidity.

Received 8th June 2020,
Accepted 26th June 2020

DOI: 10.1039/d0cy01150a

rsc.li/catalysis

1. Introduction

Owing to the adverse effects of volatile organic compounds (VOCs) on human health and environmental sustainability, their abatement before emission, especially in industrial exhausts is highly desirable.[1,2] Compared to the common treatment technologies, *e.g.*, adsorption, incineration and photocatalysis, catalytic oxidation is promising by converting VOCs into harmless products, *i.e.*, H_2O and CO_2.[3] This property attracts great attention to the development of efficient catalysts. With the merits of a low price, flexible composition, excellent redox properties, and superior thermal stability, perovskite-type oxides are considered as a promising alternative to noble metal catalysts in the oxidation of VOCs.[2] In the structure of a perovskite with the general formula ABO_3, A sites are occupied by rare earth metals (*e.g.*, La, Pr, Nd, and Sm) or alkaline earth metals (*e.g.*, Sr, Ca, and Ba), while B sites consist of transition metals (*e.g.*, Mn, Cr, Fe, Co, and Ni).[2,4] As perovskites can accommodate approximately 90% of metallic elements without structural destruction, their catalytic activity can be tuned by varying the chemical composition.[5] To date, the lanthanide perovskites $LaMO_3$ (*e.g.*, M = Mn, Co, Ni, and Fe), especially $LaCoO_3$, have been found to be greatly active towards VOC oxidation.

[a] *CAS Key Laboratory of Mineralogy and Metallogeny, Guangdong Provincial Key Laboratory of Mineral Physics and Materials, Guangzhou Institute of Geochemistry, Chinese Academy of Sciences, Guangzhou 510640, P. R. China. E-mail: liangxl@gig.ac.cn*
[b] *Guangdong Key Laboratory of Integrated Agro-environmental Pollution Control and Management, Guangdong Institute of Eco-environmental Science & Technology, Guangzhou 510650, P. R. China*
[c] *National-Regional Joint Engineering Research Center for Soil Pollution Control and Remediation in South China, Guangzhou 510650, P. R. China*
[d] *School of Environment and Energy, South China University of Technology, Guangzhou 510006, China. E-mail: liupeng@scut.edu.cn*
[e] *School of Earth and Atmospheric Sciences, Queensland University of Technology (QUT), 2 George Street, Brisbane, QLD 4001, Australia*
[f] *Institutions of Earth Science, University of Chinese Academy of Sciences, Beijing 100049, P. R. China*
[g] *University of Chinese Academy of Sciences, Beijing 100049, P. R. China*
† Electronic supplementary information (ESI) available. See DOI: 10.1039/d0cy01150a

Compared to that of noble metals, the activity of $LaMO_3$ is still less satisfactory. Meanwhile, perovskite $LaMO_3$ contains few oxygen vacancies, which slows the migration of lattice oxygen from the bulk structure to the solid surface. Based on the MVK mechanism controlling the thermal oxidation of VOCs, the rapid transfer of oxygen is beneficial for the activation and replenishment of surface oxygen, and accelerates VOC oxidation. Moreover, oxygen vacancies also facilitate the transformation of H_2O into surface hydroxyl groups, enhancing the VOC oxidation.[6] In industrial exhaust gas, water vapor is considered to inhibit the catalytic activity and stability by blocking active sites.[7] Thus, the design of catalysts with more oxygen vacancies appears as a conceivable strategy to improve catalytic performance.

Metal substitution is a typical strategy to generate oxygen vacancies in perovskites. Given the flexible accommodation of various metals in the perovskite structure, the incorporation of metals (*e.g.*, Ag, Pd, Pt, Rh, Mg, Sr, and Ca) with non-equivalent substitution has greatly influenced the activity.[2,8] The noble metal ions in a perovskite enhance the catalytic activity, such as Pd^{2+} and Ag^{+},[9,10] but they diffuse from the bulk towards the surface and form metal nanoparticles at high temperature. Compared to noble metals, non-noble metals are cheap and the obtained perovskite is stable.

However, the modification effect and mechanism vary with the type of non-noble metal at A sites or B sites. The improvement by substituting Mg at A sites in $LaMnO_3$ is ascribed to the increase in the average oxidation state of Mn, oxygen vacancies and surface oxygen species, while a negative effect is induced by the substitution of Sr, owing to the decrease in surface adsorbed oxygen and low-temperature reducibility.[8] Due to their similar radii, Ca usually substitutes La at A sites in $LaFeO_3$, $LaNiO_3$, and $LaMnO_3$ perovskites.[11] Pecchi *et al.* reported that the increased activity of the Ca-substituted $LaFeO_3$ perovskite was associated with a synergy between the pair Fe^{4+}/Fe^{3+} and the oxygen vacancies, whereas the decreased activity of the Ca-substituted $LaNiO_3$ was ascribed to the reduction in the number of active Ni^{3+}.[12] However, there are few reports regarding the effect of Ca substitution on $LaCoO_3$ in catalytic oxidation of non-methane VOCs.

The A sites in perovskites are generally inactive sites,[13] and are exclusively exposed on the perovskite surface and terminated to the detriment of the B sites.[14] This results in the possibility that the true catalytic properties of various perovskites based on ideal bulk-like terminated surfaces have been underestimated.[15] Thus, tuning perovskite particles to expose more B-sites appears feasible as an approach to enhance catalytic activity. To date, surface treatment with an acid or a base has been found to be efficient.[16–19] Li and co-workers reported an etching method with HNO_3 to selectively remove La^{3+} from $LaMnO_3$, which displayed a substantially better activity for CO oxidation than the pristine perovskite.[16] However, the strong acid treatment inevitably destroyed the perovskite structure, while the obtained γ-MnO_2 catalysts tended to be distorted and even collapsed after running at relatively high temperature.[20] To improve the thermal stability of acid-etched $LaCoO_3$, the utilization of a mild acid has been worthy of investigation. Moreover, as high-concentration water vapor may influence the catalytic stability of $LaCoO_3$, the effect of metal substitution and acid treatment on the water resistance of catalysts should also be studied.

In this work, $LaCoO_3$-based catalysts were modified by Ca substitution and/or citric acid etching, which displayed an excellent catalytic activity and water resistance in the oxidation of toluene. Through state-of-the-art characterization, the mechanism behind the improvement in activity and water resistance was elucidated. The obtained results would benefit the development of perovskite-type catalysts with high performance for VOC oxidation.

2. Experimental

2.1. Catalyst synthesis

All chemicals were used as received without further purification. $La(NO_3)_3{\cdot}6H_2O$, $Ca(NO_3)_2{\cdot}H_2O$, $Co(NO_3)_3{\cdot}6H_2O$, and $C_6H_8O_7{\cdot}H_2O$ (citric acid) of chemical grade were purchased from Aladdin Ltd. (Shanghai, China). Ca substituted $LaCoO_3$ catalysts ($La_{1-x}Ca_xCoO_3$, x = 0 and 0.1) were prepared by a one-pot sol–gel method. $La(NO_3)_3{\cdot}6H_2O$, $Ca(NO_3)_2{\cdot}H_2O$, $Co(NO_3)_3{\cdot}6H_2O$, and $C_6H_8O_7{\cdot}H_2O$ (citric acid) were dissolved in a mixed solvent (V_{H_2O} : $V_{Ethanol}$ = 2 : 1) with a mole ratio of La^{3+} : Ca^{2+} : Co^{3+} : CA equal to $1-x$: x : 1 : 2. The obtained mixture was stirred for 30 min and sonicated for 10 min at room temperature. Then, the solution was heated to 80 °C until it became a gel, followed by the evaporation of the solvent under vacuum at 90 °C to obtain the solid precursor. Finally, the precursor was milled and subsequently calcined at 700 °C for 5 h at a heating rate of 5 °C min^{-1}.

In the acid-etching process, 1.0 g fresh $LaCoO_3$ or $La_{0.9}Ca_{0.1}CoO_3$ was suspended in 100 mL citric acid solution (1 mol L^{-1}) for 1 h at room temperature. Then, the suspension was filtered and washed with deionized water to remove residual citric acid. Afterwards, the sample was dried at 80 °C for 12 h and calcined at 400 °C for 1 h. The obtained samples were pressed, ground, and sieved to 40–60 mesh for the catalytic activity test. The $LaCoO_3$ and $La_{0.9}Ca_{0.1}CoO_3$ etched with citric acid were labelled $LaCoO_3$–CA and $La_{0.9}Ca_{0.1}CoO_3$–CA, respectively.

2.2. Catalyst characterization

The as-prepared catalysts were characterized by inductively coupled plasma atomic emission spectroscopy (ICP-AES), powder X-ray diffraction (PXRD), N_2 adsorption–desorption, X-ray photoelectron spectroscopy (XPS), electron spin resonance (ESR), hydrogen temperature programmed reduction (H_2-TPR) and temperature programmed desorption (TPD) of O_2, H_2O and CO_2. The experimental details are provided in Text S1.†

2.3. Catalytic activity test

The catalytic oxidation of toluene was performed in a conventional fixed-bed reactor in the temperature range of 100–400 °C under atmospheric pressure. First, 100.0 mg of catalyst was loaded into a quartz tube reactor (i.d. = 6 mm) supported by a porous quartz plate. Gaseous toluene was generated by flowing N_2 into liquid toluene at 0 °C. The inlet gas was composed of 1000 ppm toluene and 20 vol% oxygen balanced with N_2. The total flow rate was 100 mL min^{-1}, corresponding to a gas hourly space velocity (GHSV) of 60 000 mL g^{-1} h^{-1}. The CO_2 generation was calculated according to the following equation (eqn (1)):

$$CO_2\ \text{generation} = C_{CO_2}/C^*_{CO_2} \times 100\% \quad (1)$$

where $C^*_{CO_2}$ is the concentration of CO_2 in the effluent when the toluene is completely oxidized and C_{CO_2} is that at different temperatures. To investigate the water resistance, liquid water is introduced into the feed gas (5 vol% H_2O) with a syringe pump, while a heater is attached to the gas line to avoid condensation. Before the detection of CO_2, the water in the outlet gas was removed with concentrated sulphuric acid. The concentration of CO_2 was analysed online using a non-dispersive infrared CO_2 analyser (Beijing Huayun GXH-3010E). The apparent activation energy was calculated from Arrhenius plots and more calculation details can be found in Text S2.†

3. Results and discussion

3.1. Crystal structure, morphology and oxygen vacancies

The XRD patterns of the $LaCoO_3$-based catalysts correspond well to the standard card of the perovskite phase (PDF# 25-1060), without the presence of impurity phases, *e.g.*, Co_3O_4, La_2O_3 or CaO (Fig. 1). The high-purity phase indicates that the modification by Ca substitution and/or the citric acid treatment retain the perovskite structure. However, these modifications decrease the crystallinity, as $LaCoO_3$–CA, $La_{0.9}Ca_{0.1}CoO_3$, and $La_{0.9}Ca_{0.1}CoO_3$–CA display weaker patterns than $LaCoO_3$. Due to their similar ionic radii, Ca^{2+} (1.18 Å) prefers to substitute La^{3+} (1.22 Å) at A sites. Thus, the incorporation of Ca^{2+} into the $LaCoO_3$ perovskite structure shifts the diffraction peak of the (024) facet at 2θ = 47.4° for $LaCoO_3$ to 2θ = 47.6° for $La_{0.9}Ca_{0.1}CoO_3$.

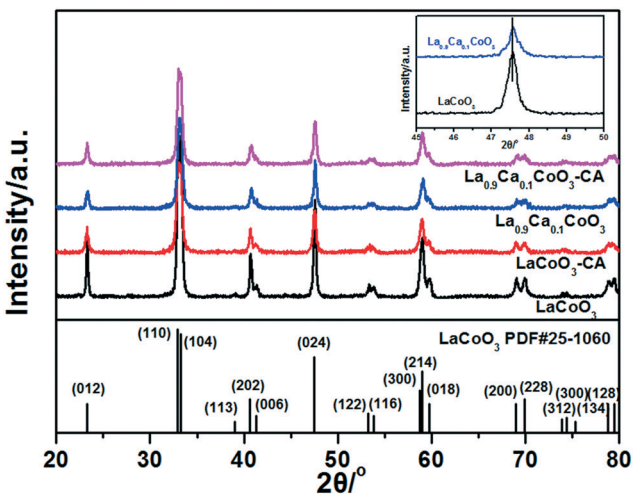

Fig. 1 XRD patterns of the $LaCoO_3$-based catalysts.

Ca substitution also inhibits the growth of crystals, as the crystallite size sharply decreases from 37.6 to 28.6 nm after Co substitution (Table 1). A similar inhibiting effect on crystal growth was also reported for $LaFeO_3$ with Ca substitution.[21] The average crystallite size of $LaCoO_3$–CA and $La_{0.9}Ca_{0.1}CoO_3$–CA is 28.6 and 25.3 nm, respectively, even smaller than those of $LaCoO_3$ (37.6 nm) and $La_{0.9}Ca_{0.1}CoO_3$ (28.2 nm). This is related to the dissolution of primary particles by citric acid. However, Ca substitution increases the structure stability of $LaCoO_3$ perovskite in citric acid etching, as the crystallite size difference between $La_{0.9}Ca_{0.1}CoO_3$ and $La_{0.9}Ca_{0.1}CoO_3$–CA is 2.9 nm, considerably smaller than that between $LaCoO_3$ and $LaCoO_3$–CA (9 nm).

ICP-AES and XPS were used to investigate the chemical composition of the bulk and on the surface of the catalysts, respectively. The surface Co/(La + Ca + Co) ratios of all the as-prepared catalysts range from 0.42–0.45, lower than the bulk value (~0.50, Table 2). This indicates that Co at B sites is less exposed on the surface than La and Ca at A sites. Such a phenomenon is also found in other La-based perovskite oxides, *e.g.*, $La_{0.5}Sr_{0.5}CoO_3$ and $La_{0.65}Sr_{0.35}MnO_3$.[14,22,23] For $La_{0.9}Ca_{0.1}CoO_3$, the surface Ca/(La + Ca + Co) (0.11) is twice that of bulk Ca/(La + Ca + Co) (0.05); thus, Ca partially enriches the surface. After citric acid etching, the surface Ca/(La + Ca + Co) of $La_{0.9}Ca_{0.1}CoO_3$ decreases from 0.11 to 0.07, while the surface La/(La + Ca + Co) of $LaCoO_3$ decreases from 0.58 to 0.55.

Based on the composition of the etching supernatant, less than 12 wt% of metals in $LaCoO_3$ and $La_{0.9}Ca_{0.1}CoO_3$ are dissolved. This suggests that the citric acid slightly etches the particles. In the etching supernatant, the La/(La + Ca + Co) of $LaCoO_3$–CA is 0.70, while the La/(La + Ca + Co) and Ca/(La + Ca + Co) of $La_{0.9}Ca_{0.1}CoO_3$–CA are 0.53 and 0.12, respectively. The La^{3+} and Ca^{2+} at A sites are more easily removed than Co^{3+} at B sites. As the aqueous Ca/(La + Ca + Co) is 2.4 times the theoretical Ca/(La + Ca + Co) (0.05) in the bulk phase, the alkali Ca^{2+} prefers to be dissolved in the citric acid solution.

Table 1 Textural properties of the $LaCoO_3$-based catalysts

Samples	[a]Crystal size/nm	[b]BET surface area/m^2 g^{-1}	[c]Pore volume/cm^3 g^{-1}
$LaCoO_3$	37.6	6	0.009
$LaCoO_3$–CA	28.6	7	0.011
$La_{0.9}Ca_{0.1}CoO_3$	28.2	9	0.019
$La_{0.9}Ca_{0.1}CoO_3$–CA	25.3	12	0.033

[a] Calculated from line broadening by the Scherrer equation. [b] Calculated from the N_2 adsorption–desorption isotherms by the multi-point BET method. [c] Calculated from the N_2 relative pressure at 0.99.

Table 2 Bulk and surface element atomic ratios of the $LaCoO_3$-based samples

	$LaCoO_3$	$La_{0.9}Ca_{0.1}CoO_3$	$LaCoO_3$–CA	$La_{0.9}Ca_{0.1}CoO_3$–CA
La/(La + Ca + Co)[a]	0.50	0.45	0.50	0.45
La/(La + Ca + Co)[b]	0.58	0.46	0.55	0.48
La/(La + Ca + Co)[c]	N/A	N/A	0.70	0.53
Co/(La + Ca + Co)[a]	0.50	0.50	0.51	0.51
Co/(La + Ca + Co)[b]	0.42	0.44	0.45	0.45
Co/(La + Ca + Co)[c]	N/A	N/A	0.30	0.35
Ca/(La + Ca + Co)[a]	N/A	0.05	N/A	0.05
Ca/(La + Ca + Co)[b]	N/A	0.11	N/A	0.07
Ca/(La + Ca + Co)[c]	N/A	N/A	N/A	0.12
O_{surf}/O_{lat}[b]	1.01	1.15	1.20	1.33
Co^{2+}/Co^{3+}[b]	0.30	0.33	0.35	0.39

[a] Average bulk element atomic ratio from ICP-AES. [b] Average surface element atomic ratio from XPS. [c] Average element atomic ratio in the etching supernatant by ICP-AES.

The effects of Ca substitution and the citric acid treatment on the morphology and microstructure of $LaCoO_3$ were observed by SEM and TEM (Fig. 2). $LaCoO_3$ displays abundant macropores connected by *ca.* 30 nm primary particles (Fig. 2a and b). After the citric acid treatment, the macroporous structure is retained (Fig. 2e and f). In contrast to $LaCoO_3$ and $LaCoO_3$–CA, $La_{0.9}Ca_{0.1}CoO_3$ shows a sheet-like morphology without obvious stacking macropores (Fig. 2i). As Ca substitution inhibits the growth of crystals, the primary particles show a rough surface (Fig. 2j).[21] Owing to the dissolution of Ca and La cations by citric acid etching, the sheet-like morphology of $La_{0.9}Ca_{0.1}CoO_3$ changes to a fluffy and

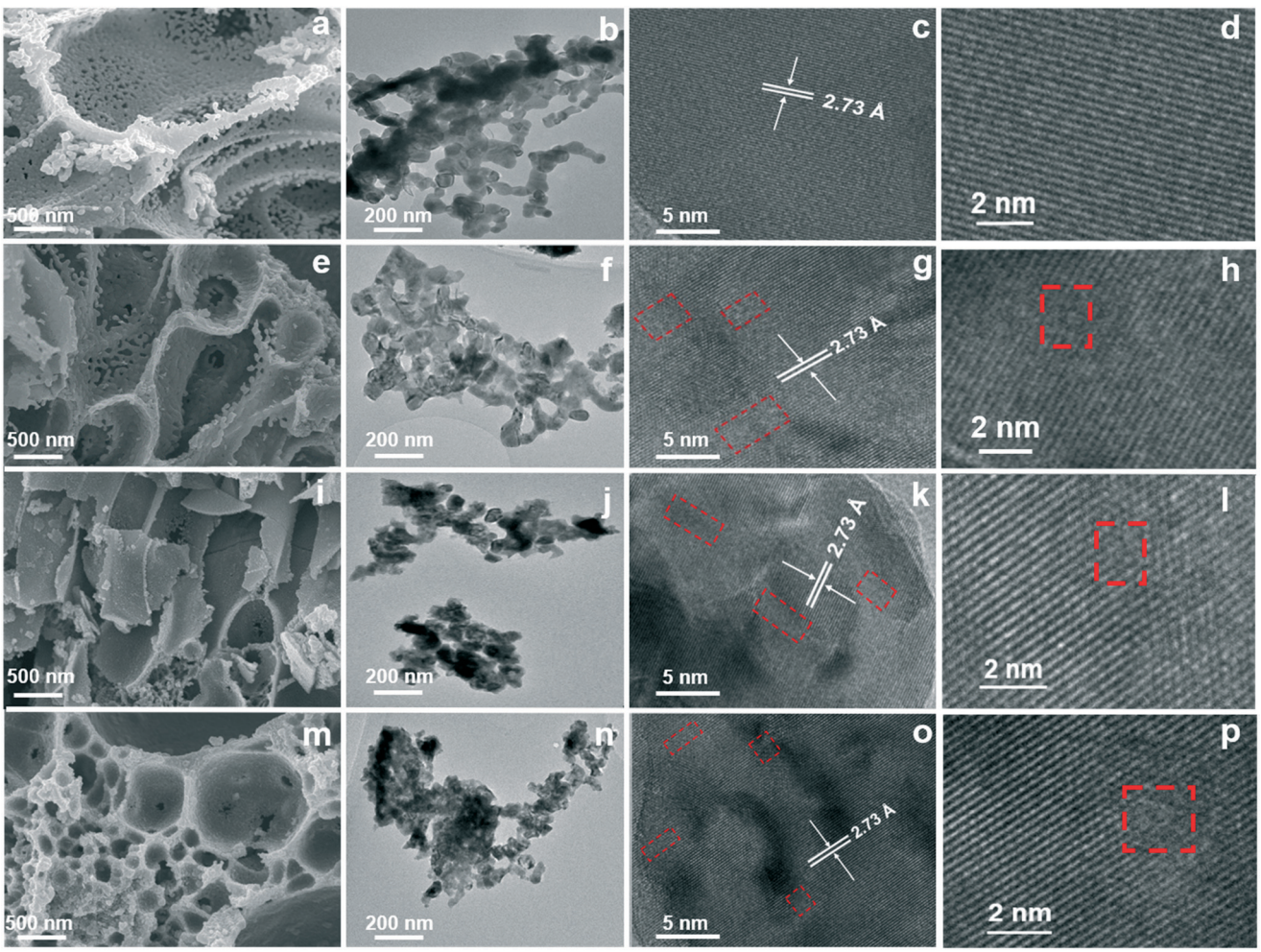

Fig. 2 SEM, TEM and HR-TEM images of $LaCoO_3$ (a–d), $LaCoO_3$–CA (e–h), $La_{0.9}Ca_{0.1}CoO_3$ (i–l) and $La_{0.9}Ca_{0.1}CoO_3$–CA (m–p).

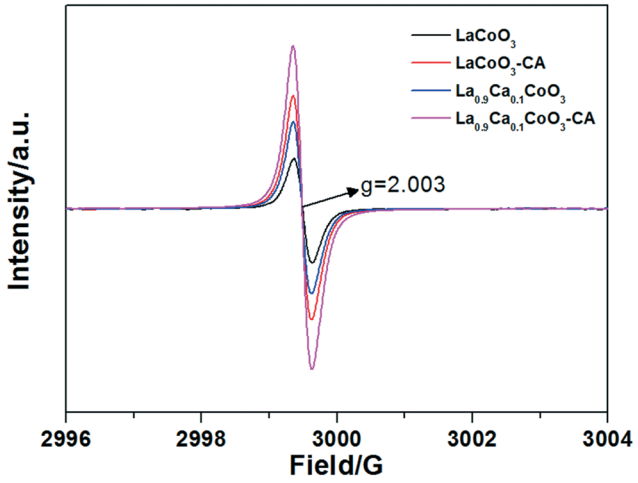

Fig. 3 ESR spectra of the $LaCoO_3$-based samples.

porous morphology (Fig. 2m), where the adhesion effect of adjacent particles becomes weak. However, $La_{0.9}Ca_{0.1}CoO_3$–CA exhibits a similar agglomerate to that in $La_{0.9}Ca_{0.1}CoO_3$, both of which are composed of dense primary particles (Fig. 2n).

For $LaCoO_3$, the well-identified lattice fringes with an interplanar distance of 2.73 Å corresponds to the (110) facet (Fig. 2c and d). The predominance of extremely regular and smooth fringes in $LaCoO_3$ throughout the whole region indicates its high crystallinity. Nevertheless, in $LaCoO_3$–CA (Fig. 2h), $La_{0.9}Ca_{0.1}CoO_3$ (Fig. 2l), and $La_{0.9}Ca_{0.1}CoO_3$–CA (Fig. 2p), certain blurry lattice fringes are observed (marked in red rectangles). According to Yang's research,[24] the blurry lattice fringes, where the array of lattice dots is discontinuous, are caused by structural defects. On the one hand, the non-equivalent substitution of La^{3+} by Ca^{2+} at A sites increases the structural disorder, leading to the production of structural defects, *i.e.*, oxygen vacancies (O_V).[18,25] On the other hand, the citric acid treatment slightly dissolves the surface of $La_{0.9}Ca_{0.1}CoO_3$, which generates surface defects on primary particles. Therefore, more obscure lattice fringes can be observed in $La_{0.9}Ca_{0.1}CoO_3$–CA.

Fig. 3 shows the ESR spectra of the $LaCoO_3$-based samples, where the g values for all the samples are 2.003. According to previous studies,[26,27] the remarkable symmetric peak is attributed to unpaired electrons at the oxygen vacancy sites, while the intensity is correlated with the concentration of O_V. The O_V amount increases apparently in the order $LaCoO_3 < La_{0.9}Ca_{0.1}CoO_3 < LaCoO_3$–CA $< La_{0.9}Ca_{0.1}CoO_3$–CA. Obviously, Ca substitution or/and the citric acid treatment increases the O_V amount. Compared to $LaCoO_3$, $La_{0.9}Ca_{0.1}CoO_3$ shows a stronger O_V signal. This is ascribed to the non-equivalent substitution of La^{3+} by Ca^{2+}.[28] Moreover, as found in the XPS analysis, the treatment by citric acid reduces Co^{3+} to Co^{2+} and generates O_V. Thus, through Ca substitution and the citric acid treatment, $La_{0.9}Ca_{0.1}CoO_3$–CA has the highest amount of O_V.

For all the catalysts, the N_2 adsorption–desorption isotherms display typical type IV characteristics with an H3 hysteresis loop (Fig. 4a). The high onset p/p_0 (0.8–1.0) of the hysteresis loop is related to the macropores and large mesopores in the agglomerates.[29] The BET specific surface area and pore volume are summarized in Table 1, both of which increase by Ca substitution and the citric acid treatment. For example, these modifications increase the specific surface area from 6.4 to 8.9 $m^2\ g^{-1}$, and the pore volume from 0.009 to 0.019 $cm^3\ g^{-1}$. Compared with the other samples, $La_{0.9}Ca_{0.1}CoO_3$–CA has a fruitful production of mesopores, with a pore width distribution centred at 30 nm (Fig. 4b), resulting from the slight etching of primary particles and the reconstruction of agglomerates (Fig. 2m–p). The increase in specific surface area and pore volume facilitates the contact of toluene with the active sites inside the pores.

XPS was carried out to study the cobalt species and oxygen species composition. The Co $2p_{3/2}$ and Co $2p_{1/2}$ binding energies are located at 780 and 795 eV, respectively (Fig. 5a). As Co is the sole multivalent metal in the as-prepared catalysts, the Co 2p spectra are deconvoluted into three components: Co^{2+}, Co^{3+}, and the shake-up peak. The peaks at *ca.* 779 and 795 eV are assigned to Co^{2+}, while the peaks at *ca.* 781 and 797 eV correspond to Co^{3+}.[30] Ca^{2+} substitution

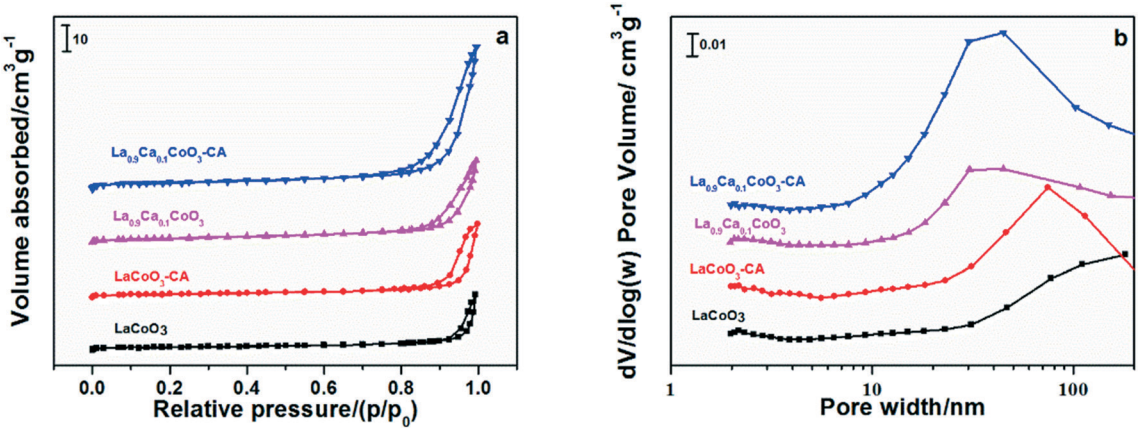

Fig. 4 N_2 sorption isotherms (a) and BJH pore size distributions (b) of the $LaCoO_3$-based samples.

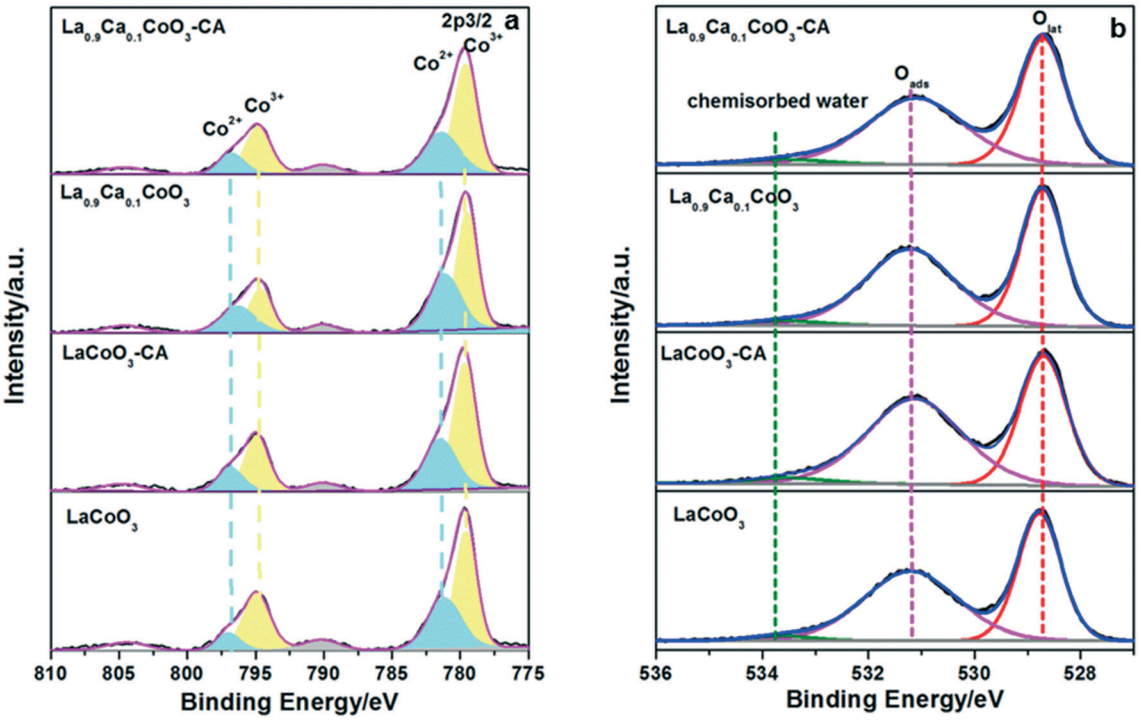

Fig. 5 Co 2p (a) and O 1s (b) XPS spectra of the $LaCoO_3$-based catalysts.

and the citric acid treatment promote the reduction of Co^{3+} (0.685 Å) to Co^{2+} (0.79 Å) to compensate for lattice contraction.[31] The generation of O_V occurs to balance the charge, which is consistent with the ESR results. The increasing trend of Co^{2+}/Co^{3+} is $LaCoO_3$ (0.30) < $La_{0.9}Ca_{0.1}CoO_3$ (0.33) < $LaCoO_3$–CA (0.35) < $La_{0.9}Ca_{0.1}CoO_3$–CA (0.39) (Table 2). The asymmetrical O 1s spectra are also deconvoluted into three symmetrical peaks at 528.6, 531.3, and 533.6 eV, which are attributed to lattice oxygen (O_{lat}), adsorbed oxygen (O_{ads}), and chemisorbed water, respectively (Fig. 5b).[32,33] The O_{ads}/O_{lat} increases apparently in the order $LaCoO_3$ (1.01) < $La_{0.9}Ca_{0.1}CoO_3$ (1.15) < $LaCoO_3$–CA (1.20) < $La_{0.9}Ca_{0.1}CoO_3$–CA (1.33) (Table 2). The increasing trend of O_{ads}/O_{lat} is the same as that of Co^{2+}/Co^{3+}. This is probably ascribed to the fact that the increase in Co^{2+}/Co^{3+} favours the formation of O_V, and accordingly the chemical adsorption of O_2 to form O_{ads} (eqn (3)). The increment in O_{ads} provides more active sites for catalytic oxidation.[34,35]

3.2. Catalytic activity towards toluene oxidation

The activity of the $LaCoO_3$-based catalysts was evaluated for the catalytic oxidation of toluene at 100–400 °C (Fig. 6a). The temperatures of 90% toluene conversion (T_{90}) over $LaCoO_3$, $La_{0.9}Ca_{0.1}CoO_3$, $LaCoO_3$–CA, and $La_{0.9}Ca_{0.1}CoO_3$–CA are 305 °C, 225 °C, 220 °C, and 202 °C, respectively. The

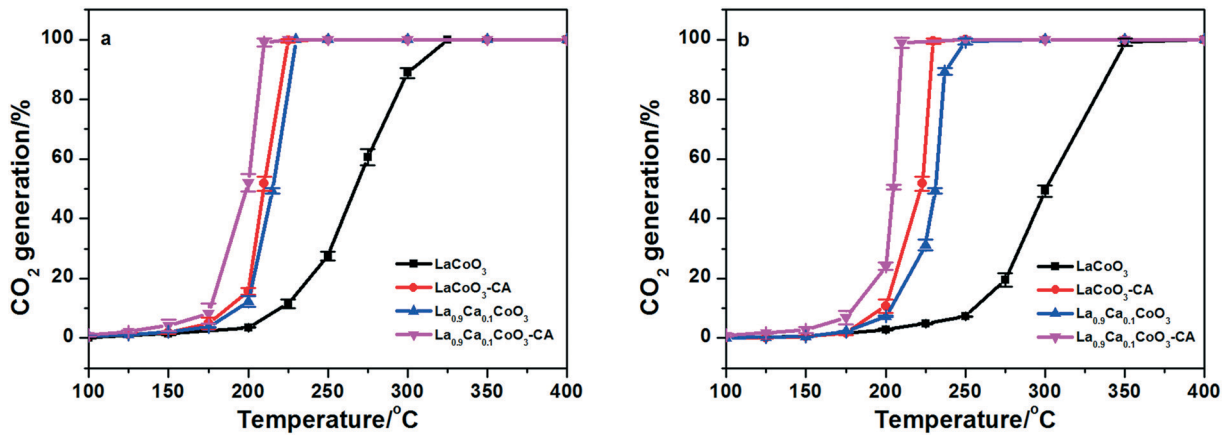

Fig. 6 The CO_2 generation over the $LaCoO_3$-based samples without H_2O (a) and with 5% H_2O (b). Reaction conditions: [toluene] = 1000 ppm, [O_2] = 20%, catalyst mass = 100.0 mg, total flow rate = 100 mL min^{-1}, and GHSV = 60 000 mL g^{-1} h^{-1}.

Table 3 Toluene oxidation activity, R_s, at 200 °C, and apparent activation energies (E_a) of the $LaCoO_3$-based catalysts

Samples	Toluene oxidation activity			R_s/μmol s^{-1} m^{-2}	E_a/kJ mol^{-1}
	T_{10}/°C	T_{50}/°C	T_{90}/°C		
$LaCoO_3$	237	268	305	0.14	62.4
$La_{0.9}Ca_{0.1}CoO_3$	194	210	220	0.31	52.3
$LaCoO_3$–CA	187	206	215	0.47	51.1
$La_{0.9}Ca_{0.1}CoO_3$–CA	187	195	202	0.63	44.1

discrepancies in the catalytic activity are further manifested by the apparent activation energy (E_a, kJ mol^{-1}, Text S2 and Fig. S1†). The E_a for toluene oxidation over the modified $LaCoO_3$ catalysts (44.1–52.4 kJ mol^{-1}) is lower than that over $LaCoO_3$ (62.4 kJ mol^{-1}) (Table 3), among which $La_{0.9}Ca_{0.1}CoO_3$–CA has the lowest E_a (44.1 kJ mol^{-1}). To exclude the influence of surface area, the specific reaction rate constant (R_s) of the $LaCoO_3$-based catalysts was calculated (Text S3,† Table 3). According to the R_s at 200 °C, the catalytic activity also increases as follows: $LaCoO_3$ (0.14 μmol s^{-1} m^{-2}) < $La_{0.9}Ca_{0.1}CoO_3$ (0.31 μmol s^{-1} m^{-2}) < $LaCoO_3$–CA (0.47 μmol s^{-1} m^{-2}) < $La_{0.9}Ca_{0.1}CoO_3$–CA (0.63 μmol s^{-1} m^{-2}). The activity sequences according to R_s at 150 and 175 °C are identical to that at 200 °C (Fig. S2†). This indicates that Ca substitution and the citric acid treatment significantly enhance the intrinsic catalytic activity of $LaCoO_3$. The catalytic activity of $La_{0.9}Ca_{0.1}CoO_3$–CA is also compared to that of reported cobalt-based catalysts (spinel and perovskite-type oxides) under similar reaction conditions (Table S1†), where the performance of $La_{0.9}Ca_{0.1}CoO_3$–CA is superior. Moreover, the catalytic activity of the $La_{0.9}Ca_{0.1}CoO_3$–CA catalyst is comparable to that of the commercial 0.5 wt% Pt/Al_2O_3 (Fig. S3†).

3.3. Structure–activity relationship

In the preparation of $La_{0.9}Ca_{0.1}CoO_3$ by the sol–gel method, Ca was easily mixed with La and Co cations in a colloidal solution, and entered the A sites of the perovskite with enrichment on the surface. The non-equivalent substitution of La^{3+} by Ca^{2+} gives rise to the formation of oxygen vacancies in the bulk perovskite. Though citric acid etching slightly dissolved the primary particles and sharply decreased the crystallinity, it also generated oxygen vacancies and removed the surface Ca^{2+} without obviously destroying the perovskite structure. The Ca substitution and/or the citric acid treatment significantly improve the catalytic performance of the perovskite $LaCoO_3$. Herein, the enhancement mechanism of these two facile modifications was carefully investigated.

The thermal catalytic oxidation of VOCs over transition metal oxides follows the Mars–van Krevelen (MVK) mechanism.[36] For the oxidation of toluene over the $LaCoO_3$-based catalysts, the oxidation process includes two-stage redox steps (eqn (2) and (3)), *i.e.*, i) the oxidation of adsorbed toluene by surface oxygen, accompanied by the reduction of Co^{3+}; ii) the re-oxidation of Co^{2+} as well as the regeneration of surface oxygen.[37]

$$-Co^{3+}-O-(s) + C_7H_8(g) \rightarrow -Co^{2+}-\square-(s) + CO_2(g) + H_2O(g) \quad (2)$$

$$-Co^{2+}-\square-(s) + O_2(g) \rightarrow -Co^{3+}-O(s) \quad (3)$$

where $-Co^{3+}-O-$ represents the surface oxygen (O_2, O_2^-, O^-, and O^{2-}) weakly or strongly bonded to Co^{3+}, and $-Co^{2+}-\square-$ indicates an oxygen vacancy. Therefore, the catalytic activity of the $LaCoO_3$-based catalysts depends on several physicochemical properties, *i.e.*, the reducibility of Co, oxygen reactivity, and desorption ability of CO_2. The reducibility and oxygen reactivity dominated the regeneration of Co^{3+}, and the feasibility of oxygen migration from the catalyst surface to CO_2 and H_2O, respectively, while the desorbability of CO_2 was related to the re-exposure of reactive sites. Thus, the above properties were analysed by H_2-TPR, O_2-TPD, and CO_2-TPD.

For the $LaCoO_3$-based catalysts, the H_2-TPR profiles exhibit two broad reduction peaks at 260–460 and 520–690 °C (Fig. 7a).

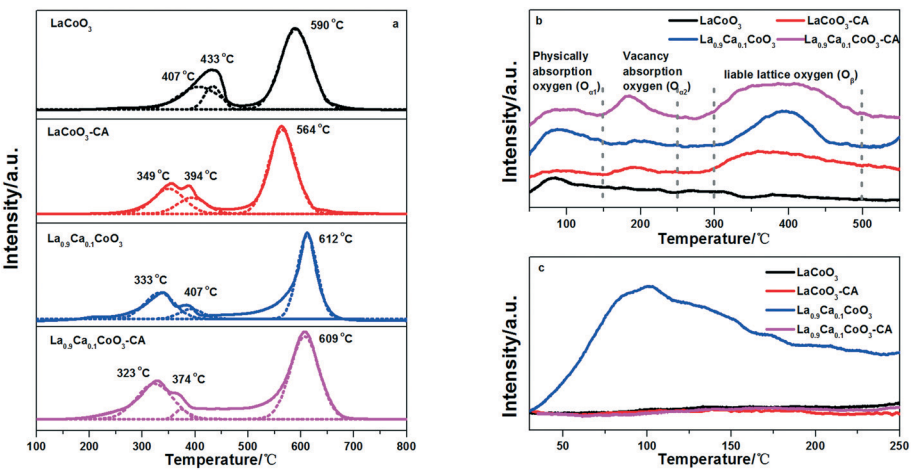

Fig. 7 H_2-TPR (a), O_2-TPD (b), and CO_2-TPD (c) profiles of the $LaCoO_3$-based catalysts.

Table 4 Reduction temperatures and H_2 consumptions of the $LaCoO_3$-based catalysts

Samples	Reduction temperature[a]/°C			H_2 consumption[b]/mmol g^{-1}			
	P_1	P_2	P_3	P_1	P_2	P_3	Total
$LaCoO_3$	407	433	590	1.80	0.71	4.79	7.30
$LaCoO_3$–CA	349	394	564	1.77	0.85	4.78	7.40
$La_{0.9}Ca_{0.1}CoO_3$	333	407	612	1.63	0.79	4.92	7.34
$La_{0.9}Ca_{0.1}CoO_3$–CA	323	374	609	1.85	0.90	4.72	7.47

[a] Reduction temperatures corresponding to the maximum values of reduction peaks in the H_2-TPR result. [b] H_2 consumptions calculated from reduction peak areas.

The first peak is related to the reduction of Co^{3+} to Co^{2+},[38] while the second one is assigned to the reduction of Co^{2+} to Co^0 (P_3).[39] The former reduction is involved in the oxidation of toluene rather than the latter one. Thus, the analysis focuses on the variation in the reduction peak at low temperature. After Ca substitution and/or citric acid etching, the reduction peak shifts to the low-temperature region, and interestingly, is split into two peaks. This implies the presence of two Co^{3+} species. According to the TEM and XPS analyses, the first peak with a high intensity is probably attributed to the reduction of Co^{3+} around/neighbouring oxygen vacancies (P_1), while the second one with a low intensity is associated with the reduction of lattice Co^{3+} (P_2). Co^{3+} around/neighbouring vacancies with lower reduction temperature has higher activity than lattice Co^{3+}. Its reduction temperature decreases as follows: $LaCoO_3$ (407 °C) > $LaCoO_3$–CA (349 °C) > $La_{0.9}Ca_{0.1}CoO_3$ (333 °C) > $La_{0.9}Ca_{0.1}CoO_3$–CA (323 °C). This is probably ascribed to the weaker Co–O bond. Moreover, the increase in surface area and pore volume also facilitates the contact between H_2 and Co^{3+}. The second reduction peaks of $LaCoO_3$, $LaCoO_3$–CA, $La_{0.9}Ca_{0.1}CoO_3$, and $La_{0.9}Ca_{0.1}CoO_3$–CA are centred at 590, 564, 612, and 609 °C, respectively. Interestingly, this reduction peak shifts to a higher temperature for $La_{0.9}Ca_{0.1}CoO_3$ and $La_{0.9}Ca_{0.1}CoO_3$–CA. This result indicates that the Ca substitution inhibits the reduction of Co^{2+} to Co^0. A similar phenomenon was also reported in a previous study,[40] where the reduction temperature range of Co^{2+} to Co^0 in $La_{1-x}Ca_xCoO_3$ was broadened and increased by Ca substitution.

The oxygen species composition was investigated by O_2-TPD (Fig. 7b). The peaks below 150 °C and in the range of 150–250 °C are attributed to the desorption of physically adsorbed oxygen ($O_{\alpha1}$) and active oxygen species on surface vacancies ($O_{\alpha2}$), respectively, while the peak in the range of 300–500 °C is attributed to the desorption of labile lattice oxygen (O_β).[32] As the desorption temperatures of $O_{\alpha2}$ and O_β are located in the temperature range of toluene oxidation, both oxygen species can be released from the catalyst to oxidize toluene during the reaction. However, compared to $O_{\alpha1}$ or O_β, $O_{\alpha2}$ species including adsorbed O_2^- and O^- are rather reactive.[33] For $LaCoO_3$, little desorption of O_α and O_β is observed, while the modified catalysts show the obvious desorption of O_β. Generally, compared to the citric acid treatment, Ca substitution generates more bulk O_V, which acts as an "oxygen channel" for the labile lattice oxygen to traverse. Thus, $La_{0.9}Ca_{0.1}CoO_3$ displays substantially more O_β desorption than $LaCoO_3$–CA. Based on the desorption amount of $O_{\alpha2}$, the order of oxygen reactivity is: $LaCoO_3$ (4.9 μmol g^{-1}) < $La_{0.9}Ca_{0.1}CoO_3$ (19.2 μmol g^{-1}) < $LaCoO_3$–CA (24.3 μmol g^{-1}) < $La_{0.9}Ca_{0.1}CoO_3$–CA (49.3 μmol g^{-1}). Among the catalysts, $La_{0.9}Ca_{0.1}CoO_3$–CA with the highest amount of O_V exhibits the most intense desorption peak of O_α.

CO_2 desorption plays a crucial role in the regeneration of catalytic sites, as CO_2 is a main product in the oxidation of toluene and may block the active sites. $LaCoO_3$, $LaCoO_3$–CA, and $La_{0.9}Ca_{0.1}CoO_3$–CA exhibit a similar CO_2 desorption contour from 30 to 250 °C (Fig. 7c). However, $La_{0.9}Ca_{0.1}CoO_3$ displays a strong CO_2 desorption peak centred at 125 °C. The order of desorption amount of CO_2 is: $La_{0.9}Ca_{0.1}CoO_3$ (15.5 μmol g^{-1}) > $LaCoO_3$ (0.60 μmol g^{-1}) > $LaCoO_3$–CA (0.58 μmol g^{-1}) > $La_{0.9}Ca_{0.1}CoO_3$–CA (0.20 μmol g^{-1}). The desorption amount of CO_2 of $La_{0.9}Ca_{0.1}CoO_3$ is significantly larger than that of the other samples. Ca substitution promotes the formation of more basic sites. These basic sites have a high adsorption capacity for the generated CO_2 and inhibit the regeneration of the active sites.[41] After citric acid etching, most basic sites are removed, resulting in a significant decrease in CO_2 desorption on $La_{0.9}Ca_{0.1}CoO_3$. The $LaCoO_3$ modified only by Ca substitution has improved CO_2 adsorption, and thus, the improvement in catalytic activity is limited.

Based on H_2-TPR, O_2-TPD, and CO_2-TPD characterization, the enhancement from Ca substitution and the citric acid treatment of the activity of $LaCoO_3$ perovskite for toluene oxidation is explained. As shown in toluene oxidation, the increasing order of R_s is: $LaCoO_3$ < $La_{0.9}Ca_{0.1}CoO_3$ < $LaCoO_3$–CA < $La_{0.9}Ca_{0.1}CoO_3$–CA. Due to the non-equivalent substitution of La^{3+} by Ca^{2+}, and accordingly the weakening of Co–O bonds, Ca substitution enhances oxygen vacancies and the low-temperature reducibility, resulting in an

Table 5 The quantitative result of the O_2-TPD profiles for the $LaCoO_3$-based catalysts

Samples	$O_{\alpha1}$/μmol g^{-1}	$O_{\alpha2}$/μmol g^{-1}	O_β/μmol g^{-1}
$LaCoO_3$	27.7	4.9	0.6
$La_{0.9}Ca_{0.1}CoO_3$	32.1	19.2	97.2
$LaCoO_3$–CA	63.8	24.3	92.8
$La_{0.9}Ca_{0.1}CoO_3$–CA	77.4	49.3	137.7

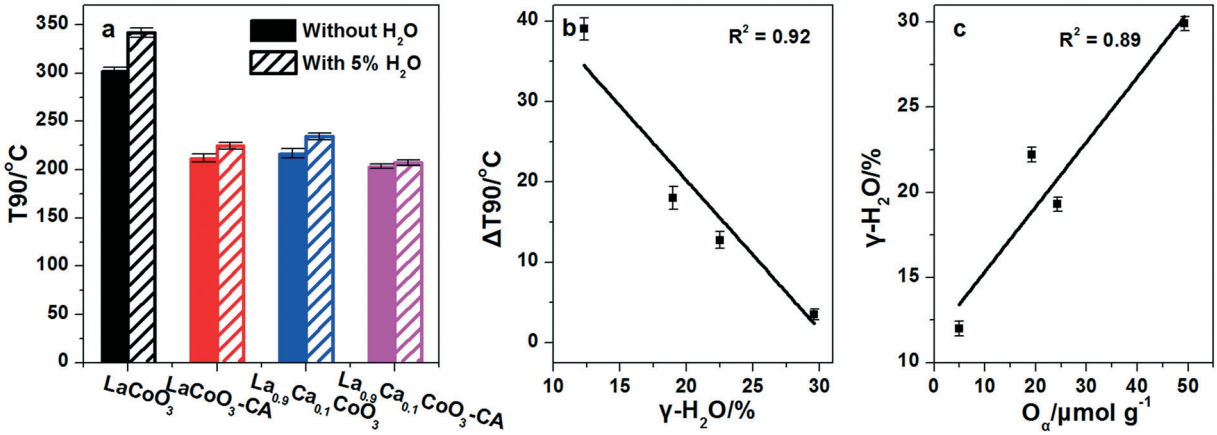

Fig. 8 The T_{90} of the $LaCoO_3$-based samples with/without the presence of 5% H_2O (a), the relationship between the γ-H_2O and ΔT_{90} (b), and the relationship between the O_α desorption quantity and γ-H_2O (c).

improvement in activity. However, the increase in basic sites inhibits CO_2 desorption. Compared to Ca substitution, citric acid etching exposes more Co cations on the perovskite surface and generates more oxygen vacancies. This action accordingly increases the amount of surface active oxygen. Both of which further improves the activity of $LaCoO_3$. When $LaCoO_3$ is treated by both citric acid etching and Ca substitution, the low-temperature reducibility and adsorption of surface oxygen enhances obviously. Moreover, most basic sites are removed, resulting in a significant decrease in CO_2 desorption on $La_{0.9}Ca_{0.1}CoO_3$–CA. Thus, $La_{0.9}Ca_{0.1}CoO_3$–CA displays the highest activity (Tables 3 and 5).

3.4. H_2O resistance

Most industrial processes produce exhaust gas containing water vapor, which suppresses the catalytic activity, especially in the low-temperature range (<300 °C). Herein, 5% H_2O vapor is introduced into the reaction system to investigate the water resistance of the $LaCoO_3$-based samples (Fig. 6b). $LaCoO_3$ shows a poor resistance to water vapor, as T_{90} increases from 305 to 345 °C. The Ca substitution and/or the citric acid treatment enhances the H_2O resistance (Fig. 8a). For example, the T_{90} of $La_{0.9}Ca_{0.1}CoO_3$–CA without H_2O (202 °C) is almost the same as that with 5% H_2O (205 °C). The activity discrepancy of the catalysts affected by water is expressed as ΔT_{90}, *i.e.*, the difference in T_{90} before and after the H_2O introduction. The ΔT_{90} values of $LaCoO_3$, $La_{0.9}Ca_{0.1}CoO_3$, $LaCoO_3$–CA and $La_{0.9}Ca_{0.1}CoO_3$–CA are 45 °C, 17 °C, 12 °C, and 3 °C, respectively (Fig. 8a). The temperature difference (ΔT_{50}) of $LaCoO_3$ before and after water addition is 32 °C, while it decreases to 8 °C over the $LaCoO_3$-based catalysts with Ca substitution or the citric acid treatment (Fig. S4†). This observation illustrates the improvement in the anti-water ability by Ca substitution and the citric acid treatment.

Table 6 Amounts of different types of adsorbed H_2O on the catalyst surface based on the fitted peak area on H_2O-TPD profiles

Samples	α-H_2O (%)	β-H_2O (%)	γ-H_2O (%)	δ-H_2O (%)
$LaCoO_3$	11.5	20.7	12.3	55.5
$La_{0.9}Ca_{0.1}CoO_3$	18.2	42.7	19.0	20.1
$LaCoO_3$–CA	15.2	15.3	22.5	47.0
$La_{0.9}Ca_{0.1}CoO_3$–CA	18.8	14.7	29.6	36.8

The removal of toluene was also determined to evaluate the CO_2 selectivity[42] and its variation by the H_2O introduction (Fig. S5a and b and Text S4†). Regardless of the presence of water, the CO_2 selectivity for all the $LaCoO_3$-based samples improves with the increase in reaction temperature (Fig. S5c and d†), but the introduction of H_2O decreases the CO_2 selectivity (Fig. S5c†). Compared to pristine $LaCoO_3$, the variation in CO_2 selectivity over modified $LaCoO_3$ is less significant. In particular, for $La_{0.9}Ca_{0.1}CoO_3$–CA, the change in CO_2 selectivity is the least, below 7% in the temperature range of 150–250 °C. This further illustrates the enhancement in catalytic stability by Ca substitution and the citric acid treatment.

To explore the mechanism for the improvement in the water resistance of the modified catalysts, the interaction between H_2O and the catalyst surface was investigated by H_2O-TPD (Fig. S6†). The obtained curves reveal the presence of four types of water on the catalyst surface (Fig. S6e†). These include i) H_2O that occupies the intraparticle space, without interaction with the catalyst surface (below 100 °C, α-H_2O),[43,44] ii) H_2O interacting with the surface-adsorbed water or hydroxyl through hydrogen bonding (100–150 °C, β-H_2O),[45] iii) surface hydroxyl groups generated through the reaction between H_2O and active surface oxygen (150–250 °C, γ-H_2O),[45] and iv) structural hydroxides (above 250 °C, δ-H_2O).[43]

According to a previous study,[43] surface hydroxyl groups, γ-H_2O, provide active protons for toluene oxidation,[43,46] whereas α-H_2O, β-H_2O, and δ-H_2O contribute less in the oxidation of toluene.[45] For the $LaCoO_3$-based catalysts, the increasing order of γ-H_2O content is $LaCoO_3$ (12.3%) < $La_{0.9}Ca_{0.1}CoO_3$ (19.0%) < $LaCoO_3$–CA (22.5%) <

$La_{0.9}Ca_{0.1}CoO_3$–CA (29.6%) (Table 6), and is consistent with that of ΔT_{90} (Fig. 8b). The γ-H_2O content of the $LaCoO_3$-based catalysts is positively correlated to the O_α amount (Table 4 and Fig. 8c), owing to the fact that surface hydroxyls are important species of surface oxygen.[47,48]

The catalytic performance of $La_{0.9}Ca_{0.1}CoO_3$–CA towards toluene oxidation at high humidity is also compared to that of the reported Co or Mn-based catalysts under identical conditions (Table S2†). The activity of $La_{0.9}Ca_{0.1}CoO_3$–CA (T_{90} = 202 °C) is higher than that of $CoMnO_x$ (T_{90} = 250 °C),[49] $Mn_{0.3}Zr_{0.7}O_2$ (T_{90} = 233 °C),[50] 3Mn1Fe (T_{90} = 260 °C), MnO_x/Cr_2O_3 (T_{90} = 270 °C),[51] and CoO_x/CeO_2 (T_{90} = 225 °C),[52] and even higher than that of noble metal catalysts, such as Pd–CoAlO (T_{90} = 240 °C)[53] and Pt–AAO (T_{90} = 230 °C).[54] Apart from the excellent water resistance, the $La_{0.9}Ca_{0.1}CoO_3$–CA catalyst also displays a satisfactory stability (Fig. S7†). In light of the strong activity, excellent stability and water resistance, $La_{0.9}Ca_{0.1}CoO_3$–CA shows promise for application in the oxidation of high-concentration industrial toluene at high humidity.

4. Conclusion

In this study, the effects of Ca substitution and/or citric acid-etching on the structural characteristics, physicochemical properties, and catalytic activity of $LaCoO_3$ were investigated. Both Ca substitution and citric acid etching improve the catalytic activity of $LaCoO_3$ towards toluene oxidation. However, the enhancement mechanisms are different.

1. Citric acid slightly etches the surface of $LaCoO_3$, so $LaCoO_3$–CA retains its macroporous morphology and a low specific surface area (7 m^2 g^{-1}). However, $LaCoO_3$–CA presents more oxygen vacancies than $LaCoO_3$, which enhances the adsorption of oxygen species and low-temperature reducibility. As a result, the T_{50} of $LaCoO_3$–CA falls from 268 to 206 °C and the apparent activation energy decreases from 62.4 to 51.1 kJ mol^{-1}.

2. The non-equivalent substitution of La^{3+} by Ca^{2+} increases the specific surface area to 9 m^2 g^{-1} and boosts the low-temperature reducibility, which is beneficial for the oxidation of toluene. However, the newly formed basic sites inhibit the desorption of the oxidation product, *i.e.* CO_2. Thus, $La_{0.9}Ca_{0.1}CoO_3$ with a worse low-temperature reducibility exhibits a higher T_{50} (210 °C) than $LaCoO_3$–CA (206 °C).

3. After the citric acid etching of the Ca-substituted $LaCoO_3$ perovskite, the catalyst exhibits a higher specific surface area, fluffy and porous morphology, and smaller crystallite size. Citric acid slightly dissolves the primary particles and prefers to remove the surface Ca^{2+}, which increases the number of oxygen vacancies and enhances the desorption of CO_2. Among the prepared catalysts, $La_{0.9}Ca_{0.1}CoO_3$–CA displays the lowest T_{50} at 195 °C for the catalytic oxidation of toluene. Moreover, the water resistance of $La_{0.9}Ca_{0.1}CoO_3$–CA is also enhanced by forming more active hydroxyl groups with a high moisture environment.

With the merits of a facile preparation, excellent activity, and water resistance, the perovskite-type $LaCoO_3$ modified by Ca substitution and citric acid etching exhibits promising industrial application potential.

Conflicts of interest

There are no conflicts to declare.

Acknowledgements

This is contribution No.IS-2880 from GIGCAS. This work was financially supported by the CAS Key Scientific Research Project (Grant No. QYZDJ-SSW-DQC023-2), the Pearl River S&T Nova Program of Guangzhou (Grant No. 201806010069), the Natural Science Foundation for Distinguished Young Scientists of Guangdong Province (Grant No. 2020B1515020015), the Guangdong Special Branch Plans (Grant No. 201629015), and the Youth Innovation Promotion Association CAS (Grant No. Y201863).

References

1 R. Atkinson and J. Arey, *Chem. Rev.*, 2003, **103**, 4605–4638.
2 S. Royer, D. Duprez, F. Can, X. Courtois, C. Batiot-Dupeyrat, S. Laassiri and H. Alamdari, *Chem. Rev.*, 2014, **114**, 10292–10368.
3 P. Liu, G. L. Wei, H. P. He, X. L. Liang and H. L. Chen, *Appl. Surf. Sci.*, 2019, **464**, 287–293.
4 Y. F. Rao, F. M. Han, Q. Chen, D. Wang, D. Xue, H. Wang and S. Y. Pu, *Chemosphere*, 2019, **218**, 299–307.
5 J. J. Zhu, H. L. Li, L. Y. Zhong, P. Xiao, X. L. Xu, X. G. Yang, Z. Zhao and J. L. Li, *ACS Catal.*, 2014, **4**, 2917–2940.
6 J. L. Wang, P. Y. Zhang, J. G. Li, C. J. Jiang, R. Yunus and J. Kim, *Environ. Sci. Technol.*, 2015, **49**, 12372–12379.
7 F. Y. Hu, J. J. Chen, Y. Peng, H. Song, K. Z. Li and J. H. Li, *Chem. Eng. J.*, 2018, **331**, 425–434.
8 C. H. Zhang, W. C. Hua, C. Wang, Y. L. Guo, Y. Guo, G. Z. Lu, A. Baylet and A. Giroir-Fendler, *Appl. Catal., B*, 2013, **134**, 310–315.
9 Y. Nishihata, J. Mizuki, T. Akao, H. Tanaka, M. Uenishi, M. Kimura, T. Okamoto and N. Hamada, *Nature*, 2002, **418**, 164–167.
10 H. L. Chen, G. L. Wei, X. L. Liang, P. Liu, H. P. He, Y. F. Xi and J. X. Zhu, *Appl. Surf. Sci.*, 2019, **489**, 905–912.
11 R. Subasri, D. Matusch, H. Nafe and F. Aldinger, *J. Eur. Ceram. Soc.*, 2004, **24**, 129–137.
12 G. Pecchi, M. Jiliberto, E. Delgado, L. Cadús and J. Fierro, *J. Chem. Technol. Biotechnol.*, 2011, **86**, 1067–1073.
13 R. J. H. Voorhoeve, D. W. Johnson, J. P. Remeika and P. K. Gallagher, *Science*, 1977, **195**, 827–833.
14 D. Neagu, G. Tsekouras, D. N. Miller, H. Menard and J. T. S. Irvine, *Nat. Chem.*, 2013, **5**, 916–923.
15 K. K. Huang, X. F. Chu, L. Yuan, W. C. Feng, X. F. Wu, X. Y. Wang and S. H. Feng, *Chem. Commun.*, 2014, **50**, 9200–9203.
16 W. Z. Si, Y. Wang, Y. Peng and J. H. Li, *Angew. Chem., Int. Ed.*, 2015, **54**, 7954–7957.
17 W. Z. Si, Y. Wang, S. Zhao, F. Y. Hu and J. H. Li, *Environ. Sci. Technol.*, 2016, **50**, 4572–4578.
18 Q. L. Yang, D. Wang, C. Z. Wang, X. F. Li, K. Z. Li, Y. Peng and J. H. Li, *Catal. Sci. Technol.*, 2018, **8**, 3166–3173.

19 Y. J. Luo, K. C. Wang, J. C. Zuo, Q. R. Qian, Y. X. Xu, X. P. Liu, H. Xue and Q. H. Chen, *Catal. Sci. Technol.*, 2017, **7**, 496–501.
20 S. H. Liang, F. T. G. Bulgan, R. L. Zong and Y. F. Zhu, *J. Phys. Chem. C*, 2008, **112**, 5307–5315.
21 S. Palimar, S. D. Kaushik, V. Siruguri, D. Swain, A. E. Viegas, C. Narayana and N. G. Sundaram, *Dalton Trans.*, 2016, **45**, 13547–13555.
22 H. Dulli, P. A. Dowben, S. H. Liou and E. W. Plummer, *Phys. Rev. B: Condens. Matter Mater. Phys.*, 2000, **62**, 14629–14632.
23 Y. Peng, W. Z. Si, J. M. Luo, W. K. Su, H. Z. Chang, J. H. Li, J. M. Hao and J. Crittenden, *Environ. Sci. Technol.*, 2016, **50**, 6442–6448.
24 X. W. Yang, Q. Gao, Z. Y. Zhao, Y. L. Guo, Y. Guo, L. Wang, Y. S. Wang and W. C. Zhan, *Appl. Catal., B*, 2018, **239**, 373–382.
25 J. I. Jung, H. Y. Jeong, J. S. Lee, M. G. Kim and J. Cho, *Angew. Chem., Int. Ed.*, 2014, **53**, 4582–4586.
26 X. L. N. Zhang, H. Ye, S. Chen, H. Ju, D. Liu, Y. Lin, W. Ye, C. Wang, Q. Xu, J. Zhu, L. Song, J. Jiang and Y. Xiong, *J. Am. Chem. Soc.*, 2016, **138**, 8928–8935.
27 Q. Z. S. Mo, J. Li, Y. Sun, Q. Ren, S. Zou, Q. Zhang, J. Lu, M. Fu, D. Mo, J. Wu, H. Huang and D. Ye, *Appl. Catal., B*, 2020, **264**, 118464.
28 Y. F. Zhao, J. Q. Zhang, W. J. Wu, X. Guo, P. Xiong, H. Liu and G. X. Wang, *Nano Energy*, 2018, **54**, 129–137.
29 F. Kleitz, F. Berube, R. Guillet-Nicolas, C. M. Yang and M. Thommes, *J. Phys. Chem. C*, 2010, **114**, 9344–9355.
30 N. A. Merino, B. P. Barbero, P. Eloy and L. E. Cadus, *Appl. Surf. Sci.*, 2006, **253**, 1489–1493.
31 R. L. Fomekong and B. Saruhan, *Front. Mater.*, 2019, **6**, 252.
32 C. H. Zhang, C. Wang, W. C. Zhan, Y. L. Guo, Y. Guo, G. Z. Lu, A. Baylet and A. Giroir-Fendler, *Appl. Catal., B*, 2013, **129**, 509–516.
33 H. Arandiyan, H. X. Dai, J. G. Deng, Y. Wang, H. Y. Sun, S. H. Xie, B. Y. Bai, Y. X. Liu, K. M. Ji and J. H. Li, *J. Phys. Chem. C*, 2014, **118**, 14913–14928.
34 Z. Wang, W. Z. Wang, L. Zhang and D. Jiang, *Catal. Sci. Technol.*, 2016, **6**, 3845–3853.
35 C. Wei, Z. X. Feng, G. G. Scherer, J. Barber, Y. Shao-Horn and Z. C. J. Xu, *Adv. Mater.*, 2017, **29**, 1606800.
36 N. N. Nassar, A. Hassan and G. Vitale, *Appl. Catal., A*, 2014, **484**, 161–171.
37 C. Doornkamp and V. Ponec, *J. Mol. Catal. A: Chem.*, 2000, **162**, 19–32.
38 X. W. Li, H. X. Dai, J. G. Deng, Y. X. Liu, S. H. Xie, Z. X. Zhao, Y. Wang, G. S. Guo and H. Arandiyan, *Chem. Eng. J.*, 2013, **228**, 965–975.
39 H. Liang, Y. X. Hong, C. Q. Zhu, S. H. Li, Y. Chen, Z. L. Liu and D. Q. Ye, *Catal. Today*, 2013, **201**, 98–102.
40 N. A. Merino, B. P. Barbero, P. Grange and L. E. Cadus, *J. Catal.*, 2005, **231**, 232–244.
41 Y. Liu, H. Zhou, R. Cao, X. Liu, P. Zhang, J. Zhan and L. Liu, *Appl. Catal., B*, 2019, **245**, 569–582.
42 J. Wang, A. Yoshida, P. F. Wang, T. Yu, Z. D. Wang, X. G. Hao, A. Abudula and G. Guan, *Appl. Catal., B*, 2020, **217**, 118941.
43 Y. H. Wang, F. Wang, Q. Song, Q. Xin, S. T. Xu and J. Xu, *J. Am. Chem. Soc.*, 2013, **135**, 1506–1515.
44 A. Setiawan, E. M. Kennedy, B. Z. Dlugogorski, A. A. Adesina and M. Stockenhuber, *Catal. Today*, 2015, **258**, 276–283.
45 C. Y. Ma, C. G. Yang, B. Wang, C. Chen, F. B. Wang, X. L. Yao and M. Y. Song, *Appl. Catal., B*, 2019, **254**, 76–85.
46 H. L. Yang, C. Y. Ma, X. Zhang, Y. Li, J. Cheng and Z. P. Hao, *ACS Catal.*, 2018, **8**, 1248–1258.
47 X. L. Weng, P. F. Sun, Y. Long, Q. J. Meng and Z. B. Wu, *Environ. Sci. Technol.*, 2017, **51**, 8057–8066.
48 X. L. Weng, Q. J. Meng, J. Liu, W. Jiang, S. Pattisson and Z. Wu, *Environ. Sci. Technol.*, 2019, **53**, 884–893.
49 W. T. Zhao, Y. Y. Zhang, X. W. Wu, Y. Y. Zhan, X. Y. Wang, C. T. Au and L. L. Jiang, *Catal. Sci. Technol.*, 2018, **8**, 4494–4502.
50 X. Q. Yang, X. L. Yu, M. Z. Jing, W. Y. Song, J. Liu and M. F. Ge, *ACS Appl. Mater. Interfaces*, 2019, **11**, 730–739.
51 X. Chen, S. C. Cai, E. Q. Yu, J. Chen and H. P. Jia, *Appl. Surf. Sci.*, 2019, **475**, 312–324.
52 F. Y. Hu, Y. Peng, J. J. Chen, S. Liu, H. Song and J. H. Li, *Appl. Catal., B*, 2019, **240**, 329–336.
53 S. Zhao, K. Z. Li, S. Jiang and J. H. Li, *Appl. Catal., B*, 2016, **181**, 236–248.
54 Q. Zhang, H. J. Luan, T. Li, Y. Q. Wu and Y. H. Ni, *Appl. Surf. Sci.*, 2016, **360**, 1066–1074.